GDCh Research Article Angewandte International Edition Chemie www.angewandte.org

How to cite: *Angew. Chem. Int. Ed.* **2025**, e202513224
doi.org/10.1002/anie.202513224

Zinc-Bromine Batteries

Taiji-Inspired Synergistic Attraction-Repulsion Electrostatic Interactions Enable Dual-Electrode Stabilization for Durable High-Areal-Capacity Aqueous Zinc-Bromine Batteries

*Qilong Wu, Rong Tang, Peiyao Wang, Fanxiang Meng, Minghao Zhang, Sirui Lin, Zeheng Lv, Jinbao Zhao, and Yang Yang**

Abstract: Aqueous zinc-bromine ($Zn-Br_2$) batteries have emerged as promising candidates for grid-scale energy storage due to their intrinsic safety and low cost. However, their practical deployment is hindered by the dissolution of polybromide species at the cathode and their subsequent shuttling and corrosive reactions at the zinc anode, which severely limit areal capacity and cycling stability. Herein, a Taiji-inspired dual-electrode stabilization strategy is developed to synergistically regulate interfacial chemistry at both electrodes, enabling durable high-areal-capacity $Zn-Br_2$ batteries. This design leverages the dynamic balance of opposing yet complementary electrostatic interactions, facilitating targeted attraction (Yin) and repulsion (Yang) of polybromides at cathode/anode interfaces, respectively. At the cathode, positively charged quaternary ammonium groups in poly(diallyldimethylammonium chloride) (PDDA) enable strong electrostatic binding to polybromides, effectively confining them within the cathode and preventing diffusion into the electrolyte. Simultaneously, a lotus-leaf-biomimetic interphase with high electronegativity and hydrophobicity is constructed on Zn anode to repel polybromides and suppress parasitic reactions. Theoretical calculations and in situ spectroscopic analyses confirm the effective suppression of polybromide shuttling and Zn corrosion. Consequently, the optimized KB-PDDA//Zn@ZnO-PFNA cell achieves a high areal capacity of 5.5 mAh cm^{-2} and exceptional cycling stability exceeding 20000 cycles, highlighting the critical importance of dual-interface engineering for advancing practical $Zn-Br_2$ battery technologies.

Introduction

Rechargeable aqueous zinc-based batteries (RAZBs) are attracting intense interest for grid-scale energy storage applications due to the intrinsic safety, environmental benignity and low cost of aqueous electrolytes.[1–5] The use of Zn metal anodes further enhances their appeal by offering a high theoretical capacity (820 mAh g^{-1}), natural abundance and excellent economic viability.[6–10] Traditional cathode materials for RAZBs are predominately manganese- and vanadium-based oxides, which rely on Zn^{2+} intercalation mechanisms. Despite significant progress in optimizing their electrochemical performance, these battery systems still suffer from fundamental limitations: 1) the divalent nature of Zn^{2+} ions induces strong electrostatic interactions with the host lattice, impeding ion diffusion and compromising structural integrity; 2) Zn^{2+} intercalation is often accompanied by proton co-insertion, resulting in local pH fluctuations that accelerate cathode dissolution and promote the formation of inactive by-products.[11,12]

To circumvent the sluggish kinetics of Zn^{2+} intercalation, halogen-based cathodes employing multi-electron conversion reactions have emerged as promising alternatives, offering higher specific capacities.[13] Zinc-iodine batteries exemplify this approach, yet their practical energy density is constrained by the relatively low redox potential (1.28 V versus Zn^{2+}/Zn for the I^-/I° couple).[14] Moreover, the high cost of iodine (~\$74 kg^{-1} based on I_2) leads to an elevated specific energy cost (\$ 0.274 Wh^{-1}), posing a significant barrier to large-scale commercialization.[15] In contrast, zinc-bromine batteries offer a more attractive alternative, featuring a higher redox potential (1.84 V versus Zn^{2+}/Zn) and enhanced specific capacity (335 mAh g^{-1} for Br_2).[16–18] Crucially, the specific energy cost of zinc-bromine ($Zn-Br_2$) systems is markedly reduced to as low as \$ 0.009 Wh^{-1}, attributed to the ultra-low cost of $ZnBr_2$ (~\$ 4.2 kg^{-1}), rendering them highly promising for scalable and cost-effective energy storage.[15,19–23] Despite these advantages, the practical implementation of $Zn-Br_2$ batteries is impeded by the dissolution and shuttling of polybromide species, which results in limited areal capacity and severe capacity fading.[24] During charging, electrochemically generated Br_2 at the cathode interacts with excess Br^- in the electrolyte to form highly soluble polybromide complexes (e.g., Br_3^- and Br_5^-).[25,26] These species readily diffuse toward the Zn anode under electric field and concentration gradients, where they participate in parasitic redox reactions,

[*] Q. Wu, R. Tang, P. Wang, F. Meng, M. Zhang, S. Lin, Z. Lv, J. Zhao, Y. Yang
State Key Laboratory of Physical Chemistry of Solid Surfaces, State-Province Joint Engineering Laboratory of Power Source Technology for New Energy Vehicle, College of Chemistry and Chemical Engineering, Xiamen University, Xiamen 361005, P.R. China
E-mail: yangyang419@xmu.edu.cn

Additional supporting information can be found online in the Supporting Information section

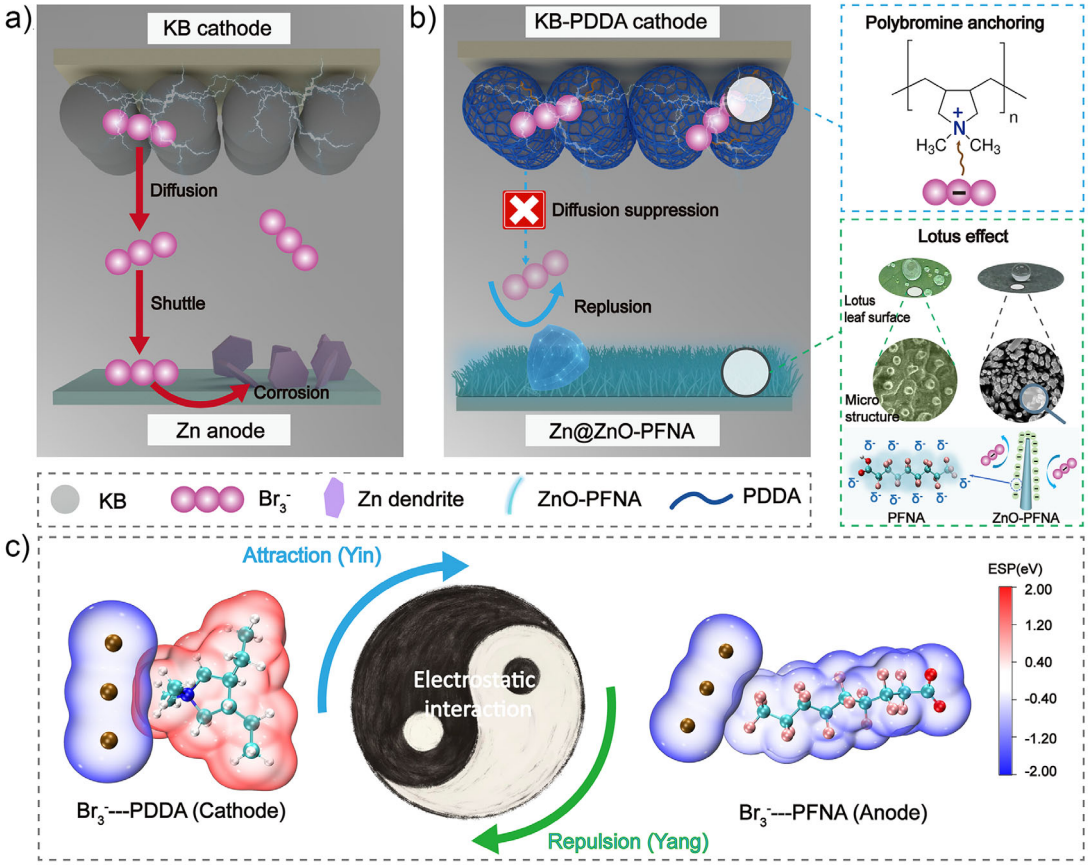

Figure 1. Schematic diagrams of a) shuttle effect of Br_3^- in Zn-Br_2 batteries, b) dual-electrode stabilization mechanism, and c) the Taiji-inspired Yin–Yang complementary electrostatic interaction strategy.

that cause Zn corrosion and accelerated capacity decay (Figure 1a).[20,27–29]

To mitigate polybromide shuttling, several strategies have been explored. One common approach involves physical confinement using porous materials such as activated carbon, metal-organic frameworks (MOFs), covalent organic frameworks (COFs), and MXenes, which immobilize polybromide species through pore trapping or interlayer adsorption.[28,30–32] However, physical absorption alone often proves insufficient for long-term operation. Another approach leverages the strong complexation affinity between polybromides and quaternary ammonium functional groups,[20,33–35] typically introduced as soluble small-molecule additives. While effective to some extent, their aqueous solubility hinders localized polybromide immobilization, especially under high areal capacity conditions (>2 mAh cm^{-2}), where polybromide generation and transport are significantly amplified. Importantly, our study reveals that polybromide species exhibit a strong specific adsorption affinity toward Zn metal. This implies that even at low bulk concentrations, polybromides can migrate to the Zn/electrolyte interface, where they are spontaneously adsorbed and initiate corrosive redox reactions. Existing strategies that focus solely on cathode or electrolyte modifications do not adequately address this interfacial vulnerability, underscoring the necessity for simultaneous regulation of both electrode interfaces.

Inspired by the traditional Chinese Taiji philosophy, we developed a dual-electrode stabilization strategy that synergistically regulates interfacial chemistry at both the cathode and anode, effectively suppressing polybromide shuttling, and Zn corrosion in high-areal-capacity Zn-Br_2 batteries. This Taiji-inspired concept embodies the dynamic balance between opposing yet complementary processes, enabling targeted attraction (Yin) and repulsion (Yang) effects toward detrimental polybromides at the cathode and anode interfaces, respectively (Figure 1c). On the cathode side, a long-chain quaternary ammonium polymer (poly(diallyldimethylammonium chloride), PDDA) is integrated with porous, conductive Ketjen Black (KB) to form a composite electrode. The abundant positively charged quaternary ammonium groups in PDDA enable strong electrostatic binding to polybromides, effectively confining them within the cathode and minimizing their diffusion into the bulk electrolyte. On the anode side, a lotus-leaf-biomimetic hydrophobic interface is constructed by in situ growth of ZnO nanorod arrays followed by surface modification with perfluorononanoic acid (PFNA). This superhydrophobic interphase combines high roughness with low surface energy, reducing direct contact with the electrolyte while introducing a negatively charged layer that electrostatically repels polybromide anions and suppresses spontaneous adsorption (Figure 1b). Consequently, the Taiji-inspired dual-interfacial regulation

enables zinc-bromine batteries to deliver a high areal capacity of 5.5 mAh cm^{-2} and an exceptional cycling stability over 20000 cycles. This work highlights the importance of simultaneously engineering both electrode interfaces to mitigate polybromide shuttling and Zn corrosion, offering valuable insights into the development of practical high-areal-capacity zinc-bromine batteries.

Results and Discussion

Degradation Mechanism of Zn-Br_2 Batteries

To comprehensively elucidate the degradation mechanism of Zn-Br_2 batteries, we conducted a visual charging experiment using a cuvette-based cell comprising a KB cathode, 2 M $ZnBr_2$ electrolyte, and a Zn foil (100 μm) anode. As shown in Figure 2a, yellow-colored species began to appear on the cathode surface after 6 min of charging and substantially dissolved into the electrolyte by 20 min. UV–vis spectroscopy (Figure 2b) identifies these species as polybromide ions (Br_n^-, $n = 2x+1$). Upon discharge, the cell exhibited a low Coulombic efficiency (CE) of only 53.7% (Figure S1), indicating severe self-discharge stemming from polybromide dissolution. To probe the corrosive interactions between polybromides and the Zn anode, in situ optical microscopy measurement was employed. As depicted in Figure 2c, Zn foil immersed in a Br_3^- solution exhibited progressive surface darkening over 12 h, directly visualizing the corrosion process. In contrast, Zn foil immersed in deionized water showed no visible change over the same period (Figure 2d), confirming the spontaneous and aggressive corrosivity of Br_3^- toward metallic Zn. Scanning electron microscopy (SEM) analysis further reveal that Zn immersed in 10 mM Br_3^- for 48 h developed a thick and porous corrosion layer with deep localized penetration and a complete loss of metallic luster (Figure 2e). By contrast, Zn in deionized water formed a much thinner and denser passivation layer (Figure 2f). To gain further insight into the formation of this corrosion morphology, in situ UV–vis spectroscopy was conducted to monitor Br_3^- concentration in real time. Immersion of Zn into 0.5 mM Br_3^- solution results in a gradual decline of the characteristic absorption peak at ~266 nm (Figure 2g), whereas a control solution without Zn exhibits negligible spectral change over 30 min (Figure S2). Additionally, ex situ UV–vis spectra further reveal a concurrent increase in the ~188 nm peak associated with Br^- (Figure S3), confirming the occurrence of following spontaneous redox reaction:

$$Zn + Br_3^- \rightarrow Zn^{2+} + 3Br^- \quad (1)$$

This reaction is believed to be initiated preferentially at Zn grain boundaries, leading to the formation of a structurally loose and porous corrosion layer.

To investigate the initial adsorption behavior, quartz crystal microbalance (QCM) measurements were performed. As shown in Figure 2h, upon the addition of 10 mM Br_3^- solution, the vibrational frequency rapidly increased by 285 Hz following the initial perturbation-induced shift, corresponding to a 399 ng decrease in the apparent electrode mass. This mass decrease is attributed to the spontaneous adsorption of Br_3^- at the Zn/electrolyte interface, which excludes H_2O molecules from the electric double layer (EDL). Density functional theory (DFT) calculations further reveal a high binding energy of −2.72 eV for Br_3^- on Zn (Figure 2j), indicating a strong specific adsorption nature. This is corroborated by molecular dynamics (MD) simulations (Figure 2i), which shows significant Br_3^- accumulation within the EDL of Zn/electrolyte interface, promoting localized reaction and corrosion. To assess the practical implications of polybromide shuttling, a KB//Zn full cell was assembled (Figure 2k). This cell exhibited a low CE of 85.5% and suffered abrupt failure after 189 cycles. Post-mortem analysis reveals Zn dendrite penetration through the separator and extensive anode corrosion, as confirmed by SEM images (Figure S4). These results indicate that the battery failure was mainly caused by internal short-circuiting, stemming from Br_3^--induced corrosion and accelerated dendritic growth.

Generally, the degradation mechanism of Zn-Br_2 batteries associated with polybromide dissolution can be categorized into three sequential processes (Figure S5). 1) During charging, polybromide ions form at the cathode and dissolve into the electrolyte, decreasing cathodic reversibility and CE. 2) Dissolved polybromides migrate toward the Zn anode under electric field and concentration gradients, resulting in the shuttle effect. 3) Upon reaching the anode region, polybromides are spontaneously adsorbed onto the Zn surface and initiate corrosive redox reactions at grain boundaries, forming a loose, porous corrosion layer that exacerbates Zn dendrite growth and leads to internal short-circuit failure. These findings emphasize that both the dissolution of polybromides from cathode into electrolyte and their subsequent adsorption onto the Zn surface are critical in governing shuttle-induced self-discharge and anode degradation. Simultaneous regulation of both interfacial processes is therefore essential to achieving stable, high-performance Zn-Br_2 batteries.

Anchoring Polybromides Through the Electrostatic Attraction

To inhibit polybromide dissolution at the cathode, a KB-PDDA composite electrode was fabricated by incorporating commercially available PDDA with KB via slurry casting. The quaternary ammonium groups in PDDA carry strong positive charges and are expected to immobilize polybromide anions through electrostatic attraction, while KB provides a high-surface-area (1253.7 m^2 g^{-1}; Figure S6) conductive framework to support efficient redox reactions. Elemental mapping of the KB-PDDA electrode reveals a smooth surface with uniform distribution of C, N, and Cl elements (Figure 3a), indicating homogeneous PDDA dispersion. The polybromide adsorption capacity was evaluated by adding equal masses of KB and PDDA into 50 mM Br_3^- solutions and equilibrating overnight. The PDDA-treated solution became nearly transparent with negligible signal Br_3^- absorbance in the UV–vis spectrum, whereas the KB-treated solution retained a yellow hue and detectable Br_3^- spectral features (Figure 3b).

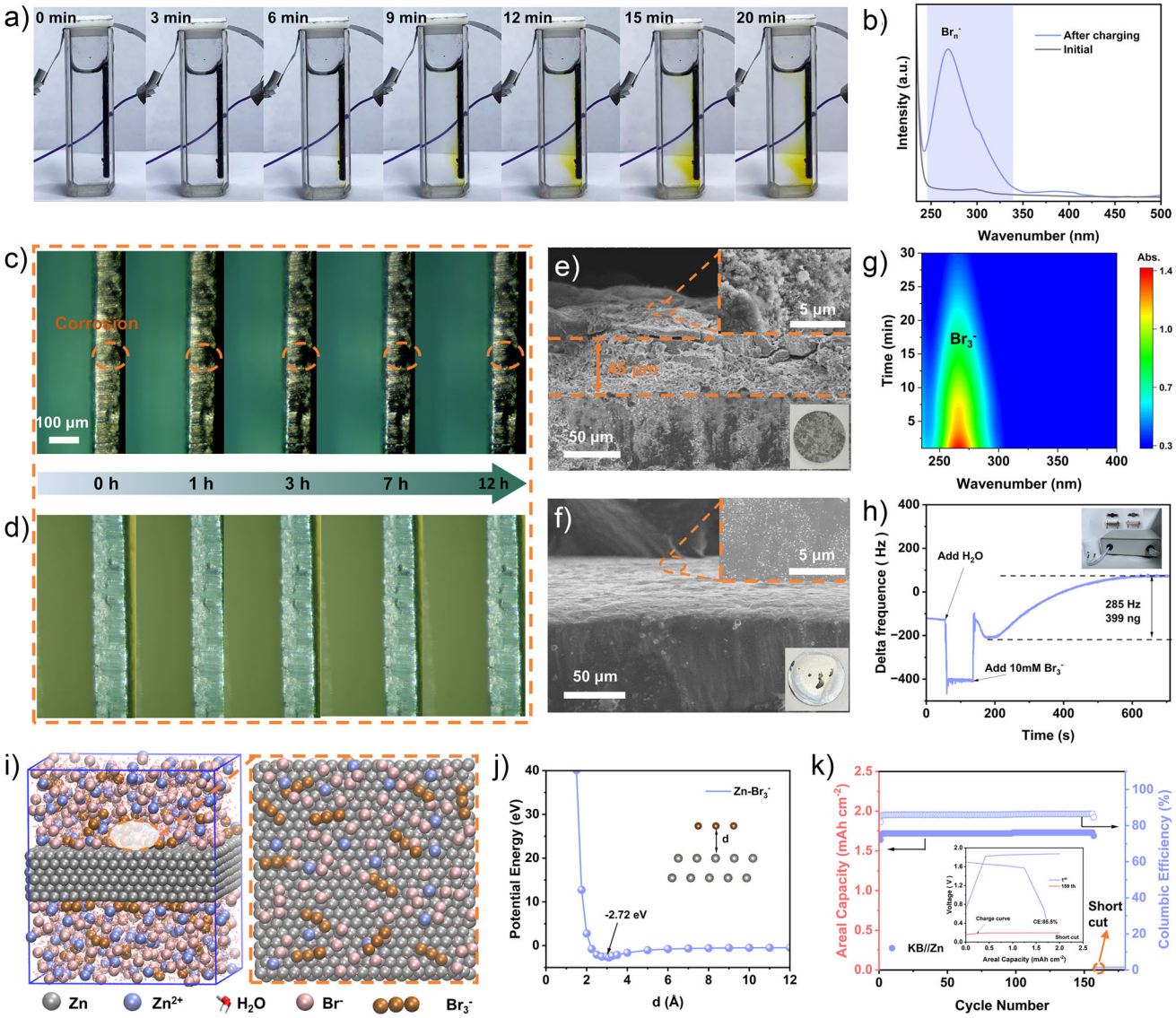

Figure 2. Deterioration mechanism of Zn-Br_2 batteries. a) Optical pictures of the Zn-Br_2 battery charged at 3 mA cm^{-2} and b) its corresponding UV–vis spectra. In situ optical microscopy images of Zn foil corroding in c) 10 mM Br_3^- solution and d) deionized water. Cross-sectional SEM images of Zn foil soaked in e) Br_3^- solution and f) deionized water for 2 days (insets are surface SEM images and pictures). g) In situ UV–vis spectra of Br_3^- solution during Zn foil immersion. h) QCM test of Br_3^-. i) MD simulations of bare Zn interface in the Br_3^- containing 2 M $ZnBr_2$ electrolyte (inset displays the specie distribution in the EDL region). j) The interaction energy of Zn and Br_3^- versus their interatomic distance. k) Cycling stability of KB//Zn battery at 50 mA cm^{-2} for 2 mAh cm^{-2} (inset is the corresponding charge/discharge curves).

Theoretical calculations (Figure 3c) show that PDDA has a strong binding energy of −4.40 eV with Br_3^-, significantly higher than that of Zn^{2+} (−1.81 eV) or H_2O (−0.28 eV). Differential charge density plots (Figure S7) further confirm pronounced electron redistribution at the PDDA/Br_3^- interface, supporting robust electrostatic interactions. In addition, zeta potential measurements demonstrate a substantial increase from +3.07 mV for KB to +56.73 mV after PDDA incorporation, indicating significantly enhanced electrostatic affinity for negatively charged Br_n^- species (Figure S8).

The electrochemical effectiveness of the KB-PDDA composite was preliminarily validated in Zn-Br_2 full cells. Cyclic voltammetry (CV) measurements show that the KB-PDDA electrode exhibits a larger cathodic peak area than pristine KB, indicating improved reversibility of the Br^-/Br_n^- conversion (Figure S9). Galvanostatic cycling at 10 mA cm^{-2} (Figure 3d) further demonstrates a marked improvement in CE from 51.3% (KB//Zn) to 96.8% (KB-PDDA//Zn), confirming effective suppression of polybromide shuttling. In situ optical visualization using Pt wires coated with KB and KB-PDDA further confirms polybromide confinement. The KB-coated wire exhibits intense color changes during charging that persist after discharge, indicative of irreversible polybromide leakage (Figure 3e). In contrast, the KB-PDDA-coated wire displays only minor color changes, which disappear after discharge (Figure 3f). Consistent behavior was also observed using conventional carbon felt current collectors (Figure S10). In situ UV–vis spectroscopy (Figure 3g) near the cathode

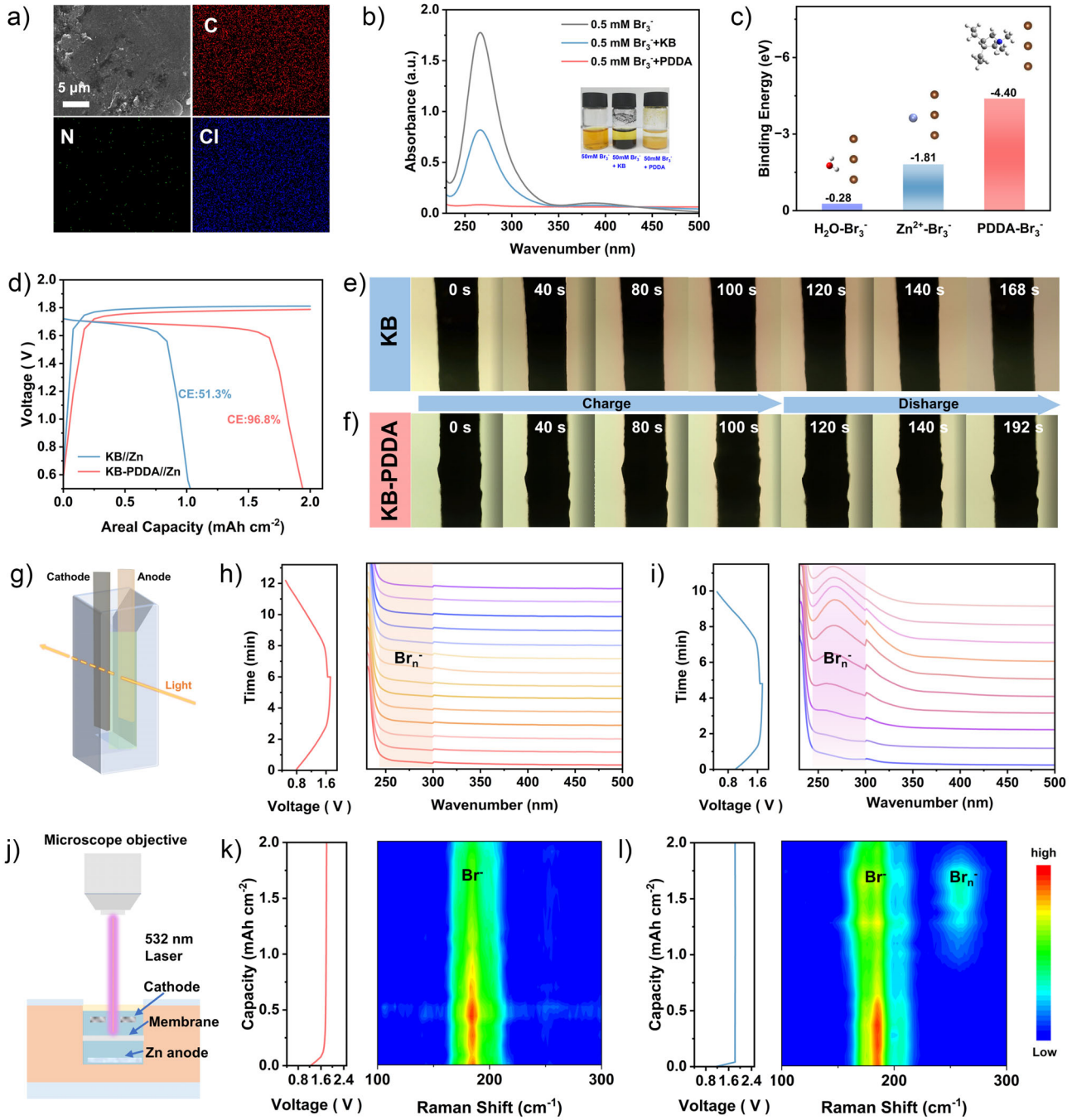

Figure 3. The mechanism of polybromide ions shuttle inhibition by PDDA. a) EDS mapping of the KB-PDDA electrode. b) UV–vis spectra. c) Binding energy of Br_3^- with Zn^{2+}, H_2O, and PDDA. d) The charge/discharge curves of KB//Zn and KB-PDDA//Zn batteries at 10 mA cm^{-2}. In situ optical microscopy observation of polybromine dissolution at e) KB electrode and f) KB-PDDA electrode. g) Schematic of quartz cuvette cell for real-time UV–vis spectroscopy testing. Real-time UV–vis spectroscopy and accompanying charge/discharge curves of h) KB-PDDA electrode and i) KB electrode. j) Diagram of a self-made electrochemical cell used for real-time Raman tests. Real-time Raman testing of k) KB-PDDA//Zn and l) KB//Zn, and corresponding charging curves.

shows sustained Br_n^- absorption bands (244~349 nm) for the KB cathode (Figure 3i), while no appreciable spectral changes were detected for KB-PDDA (Figure 3h), indicating effective polybromide confinement. Moreover, in situ Raman spectroscopy using a home-made coin-type electrochemical provides additional validation (Figure 3j). A characteristic peak at ~257 cm^{-1} attributed to Br_3^-/Br_5^- appears during charging of the KB electrode (Figure 3l) but is nearly absent for the KB-PDDA electrode (Figure 3k).[36] These results provide direct spectroscopic evidence of the strong anchoring capability of PDDA and its effectiveness in mitigating polybromide shuttling.

Repelling Residual Polybromides from EDL Through the lotus Effect

To further suppress residual polybromide leakage from the KB-PDDA cathode during extended cycling, a hydrophobic and strongly negatively charged lotus-leaf-inspired interphase was engineered on the Zn anode. This interfacial design minimizes electrolyte contact and repels Br_n^- species via electrostatic repulsion. The lotus effect is governed by two critical parameters[37]: i) high surface roughness and ii) low surface energy (Figure S11). Accordingly, a two-step strategy was employed: Zn foil was first roughened through in situ hydrothermal growth of a ZnO nanoarray, followed by surface modification with perfluorononanoic acid (PFNA). The long perfluoroalkyl chains of PFNA reduce surface energy, yielding the Zn@ZnO-PFNA structure. XRD and SEM analyses confirm the formation of rod-like ZnO nanostructures, which remain morphologically intact after PFNA treatment (Figures S12 and S13). Elemental mapping further verifies uniform distributions of Zn, O, and F, demonstrating successful surface functionalization (Figure 4a). The resulting interfacial layer is approximately 2 μm thick, which is sufficiently thin to preserve Zn^{2+} transport, as evidenced by the lower charge-transfer resistance in KB//Zn@ZnO-PFNA cell compared to that of KB//Zn cell (Figures S14 and S15). Fourier transform infrared (FTIR) spectroscopy confirms the chemical incorporation of PFNA in Zn@ZnO-PFNA (Figure 4b), with characteristic peaks assigned to asymmetric and symmetric O═C─O$^-$ stretching (1762 and 1422 cm^{-1}) and C─F bonds (1202 and 1147 cm^{-1}). The redshift in carboxylate vibrations suggests the formation of zinc perfluorononanoate. Supporting this, XRD patterns show a significant decrease in the ZnO (002)/Zn (101) intensity ratio after PFNA treatment (Figure S13), implying strong interfacial interaction. The highly electronegative C─F bonds impart a strongly negative surface charge, confirmed by a zeta potential of −25.02 mV (Figure S16), thereby establishing an effective electrostatic barrier against Br_n^- species. The surface also exhibits excellent hydrophobicity, with a contact angle of 137.8°, substantially greater than that of bare Zn (Figure 4c).

The anti-corrosion properties were evaluated using in situ UV–vis spectroscopy. As shown in Figure 4d, Br_3^- concentration undergoes a smaller change after 30 min of immersion with Zn@ZnO-PFNA, indicating less corrosion compared to bare zinc foil (Figure 2g). Tafel polarization curves reveal a higher corrosion potential and lower corrosion current density for Zn@ZnO-PFNA compared to bare Zn in Br_3^--containing electrolyte (Figure 4e). Additionally, the hydrogen evolution overpotential shifts from −0.11 V (bare Zn) to −0.15 V for Zn@ZnO-PFNA (Figure S17), suggesting suppressed HER due to reduced interfacial water activity benefitting from the lotus effect. Electrochemical stability was further assessed in symmetric Zn@ZnO-PFNA cells using 2 M $ZnBr_2$ electrolyte. These cells operated stably for over 800 h at 1 mA cm^{-2} for 1 mAh cm^{-2}, significantly outperforming bare Zn (50 h, Figure S18). Even in a mixed electrolyte containing 10 vol% 10 mM Br_3^-, the Zn@ZnO-PFNA cell maintains stable operation for over 500 h (Figure 4f), nearly 25 times longer than its unprotected counterpart (19 h).

To further investigate the influence of ZnO-PFNA interfacial layer on ion distribution, theoretical simulations were conducted. Electrostatic potential (ESP) analysis (Figure S19) indicates that the highly electronegative C─F bonds create a negatively charged surface around PFNA molecules, which attracts Zn^{2+} and repels Br_n^- through ion-dipole interactions, thereby facilitating Zn^{2+} transport while while preventing polybromide species penetration. This result was further supported by the binding energies of PFNA with Br_3^- (0.52 eV) and Zn^{2+} (−1.11 eV) (Table S1). MD simulations confirm significant Br_3^- accumulation within the Helmholtz layer of bare Zn (Figure 4i), promoting corrosion. In contrast, the potential energy of Br_3^- interacting with PFNA remains consistently positive (Figure 4g), indicative of electrostatic repulsion. As a result, Br_3^- ions are mostly excluded from the Helmholtz layer at the Zn@PFNA interface (Figures 4h,j and S20), effectively eliminating active corrosion sites. Quantitative analysis shows that the normalized density of Br_3^- in the Helmholtz layer of Zn/electrolyte is ∼3×higher than that in the bulk-phase electrolyte, whereas Br_3^- accumulation at the Zn@PFNA interface is nearly zero (Figure 4k). Dynamic snapshots further provide dynamic insights into corresponding interface behavior. The Br_3^- anion spontaneously undergoes adsorption upon approaching the metallic Zn, forming a tight binding with the Zn surface (Figure 4l), whereas they are quickly separated to maintain a certain distance from the PFNA, preserving a balanced energy state (Figure 4m). This spatial exclusion mechanism effectively suppresses interfacial corrosion initiation.

Zinc-Bromine Full Battery Electrochemical Performance

The effectiveness of the Taiji-inspired dual-interfacial regulation was systematically validated by assembling Zn-Br_2 full batteries and subjecting them to comprehensive electrochemical evaluation. As illustrated in Figure 5a, the KB-PDDA//Zn@ZnO-PFNA cell delivers a stable discharge capacity of 2.0 mAh cm^{-2} and sustains 20000 cycles with a high average CE of 98.0%. In comparison, the KB-PDDA//Zn cell delivers 7930 cycles with a slightly lower average CE of 97.1%, while the unmodified KB//Zn cell fails after only 381 cycles, accompanied by a markedly reduced CE of 79.3%. SEM images of the Zn anodes after 50 cycles reveal progressively diminished corrosion features in the dual-protected system (Figure S21). Consistently overlapped voltage-capacity profiles (Figure S22), further corroborate the interfacial stability of both electrodes. Rate performance tests (Figure S23) also demonstrate that the KB-PDDA//Zn@ZnO-PFNA cell maintains a higher CE than KB-PDDA//Zn and KB//Zn cells over a wide range of 5–50 mA cm^{-2}. Notably, negligible CE decay is observed even when the current density is abruptly decreased from 50 to 5 mA cm^{-2}, confirming its excellent rate adaptability. Even at an ultra-high current density of 50 mA cm^{-2}, the KB-PDDA//Zn@ZnO-PFNA cell still achieves a considerable discharge capacity of 2 mAh cm^{-2} for 16000 cycles (Figure S24), highlighting its outstanding high-rate cycling capability. To further demonstrate its potential for practical applications, a full cell employing an ultra-thin 10 μm

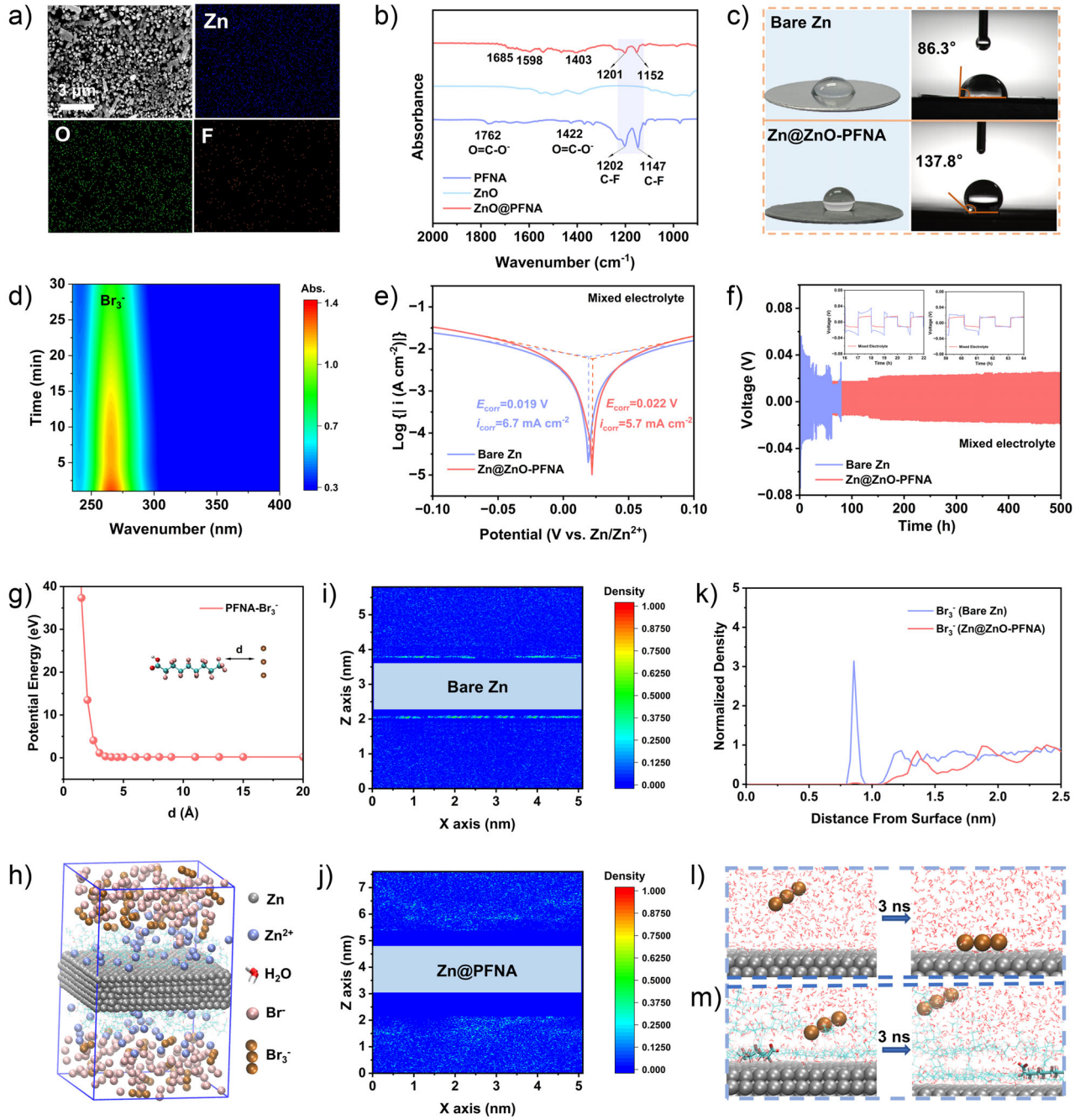

Figure 4. Physical characterization of Zn@ZnO-PFNA interfacial layer and its anti-corrosion mechanism against polybromide ions. a) EDS mapping. b) FTIR of the PFNA, ZnO and ZnO@PFNA. c) Contact angle testing. d) In situ UV–vis spectra of Br_3^- solution during Zn@ZnO-PFNA immersion. e) Tafel plots. f) Cycling performance of bare Zn and Zn@ZnO-PFNA symmetric batteries at 1 mA cm^{-2} for 1 mAh cm^{-2}. g) The interaction energy of PFNA and Br_3^- versus their interatomic distance. h) MD simulations of Zn@PFNA in the Br_3^- containing 2 M $ZnBr_2$ electrolyte. i), j) Density distribution map of Br_3^- anions in electrode/electrolyte interface. k) Normalized density profiles of Br_3^- anions in bare Zn/electrolyte and Zn@PFNA/electrolyte. l) a Br_3^- ion gradually approaching the Zn surface and m) a Br_3^- ion progressively distancing from PFNA molecules spontaneously.

Zn foil with a near-ideal n/p ratio of one was assembled (Figure 5b). Consequently, this configuration also achieves stable operation over 800 cycles, delivering a high areal capacity of 5.5 mAh cm^{-2}. As summarized in Figure 5c and Table S2, the KB-PDDA//Zn@ZnO cell outperforms most previously reported Zn-Br_2 batteries systems in terms of bromine utilization and cycle life.[14,19,25,30–32,38–43]

Moreover, the KB-PDDA//Zn@ZnO-PFNA pouch cell (18 mAh) demonstrates comparable cycling performance (~200 cycles) and CE (~97.5%) at both room temperature and 0 °C. This is could be attributed to the similar impedance and ionic conductivity at both temperatures, thus demonstrating excellent low-temperature adaptability (Figures 5d and S25; Table S3). Notably, the pouch cell continues to

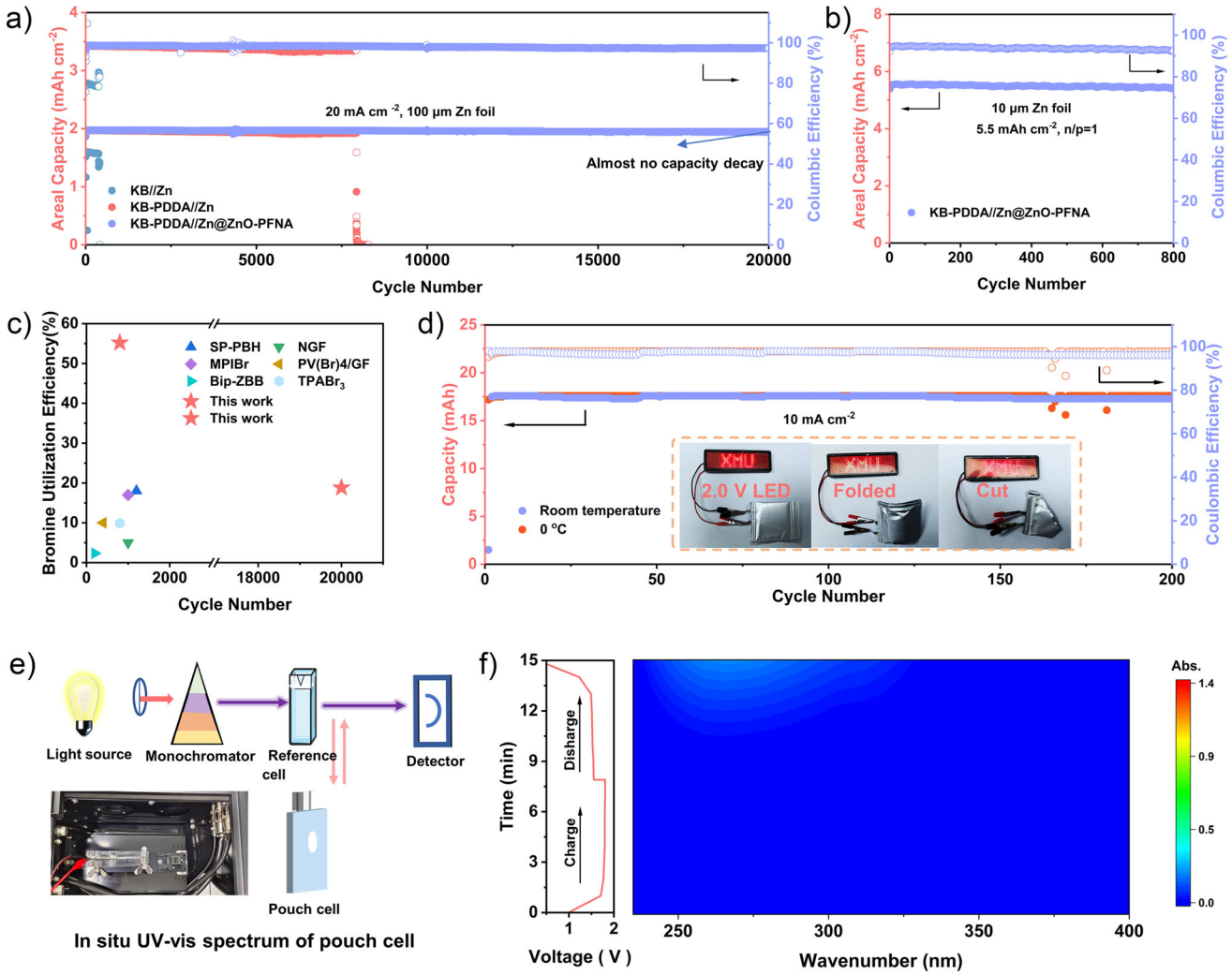

Figure 5. Electrochemical performance of Zn-Br_2 batteries. a) Cycling performance at 20 mA cm^{-2} for 2 mAh cm^{-2}. b) Long cycling performance of KB-PDDA//Zn@ZnO-PFNA batteries with a current density of 20 mA cm^{-2}, a charge capacity of 5.86 mAh cm^{-2} and n/p ratio of 1. c) The electrochemical performance compared with other reported Zn-Br_2 batteries. d) Cycling performance of the KB-PDDA//Zn@ZnO-PFNA pouch cell at 10 mA cm^{-2} under 0 °C and room temperature conditions (the inset shows pictures of the pouch cell powering an LED light). e) Schematic diagram of in situ UV–vis test of the pouch cell. f) In situ UV–vis spectra of KB-PDDA//Zn@ZnO-PFNA pouch cell and its corresponding charge/discharge curves.

power a 2 V LED even after mechanical deformation such as bending and cutting (insets in Figure 5d), highlighting its mechanical robustness. To further assess polybromide confinement under realistic working conditions, in situ UV–vis spectroscopy was conducted on the pouch cells fitted with optical windows (Figure 5e). For the KB-PDDA//Zn@ZnO-PFNA cell, no detectable polybromide species were observed throughout the charge-discharge process (Figures 5f and S26), whereas the KB//Zn pouch cell shows a strong polybromide signal that exceeds the detection range of the instrument (Figure S27). These results unequivocally validate the effectiveness of the Taiji-inspired dual-interfacial strategy in suppressing polybromide shuttling and maintaining electrochemical stability under practical operating conditions.

Conclusion

In conclusion, this study systematically identifies the dissolution of polybromide species during charging and their subsequent specific adsorption-corrosion reaction at the Zn anode as primary origin of low CE and short-circuit failure in Zn-Br_2 batteries. To address these issues, a Taiji-inspired dual-interface stabilization strategy is developed, integrating a KB-PDDA composite cathode rich in quaternary ammonium groups and a lotus-leaf-biomimetic interface on the Zn anode. The abundant positively charged quaternary ammonium groups in PDDA electrostatically anchor polybromide anions at the cathode, whereas the Zn@ZnO-PFNA layer repels them at the Zn/electrolyte interface, thereby simultaneously suppressing polybromide shuttling and parasitic reactions.

Theoretical calculations and in situ characterization corroborate the efficacy of this dual-barrier design. As a result, the KB-PDDA//Zn@ZnO-PFNA battery sustains an ultra-long cycling life of 20000 cycles at 20 mA cm^{-2} (2 mAh cm^{-2}), and shows no capacity fade over 800 cycles even at an enhanced areal capacity of 5.5 mAh cm^{-2}. In pouch-cell configuration, the battery attains a high CE of 97.5% over 200 cycles at both 0 °C and room temperature, demonstrating its potential for low-temperature practical applications. This work not only elucidates the degradation mechanism of Zn-Br_2 batteries but also provides a scalable pathway toward high-capacity, long-life, and cost-effective aqueous Zn-Br_2 battery systems.

Acknowledgements

The authors gratefully acknowledge the financial support from the National Natural Science Foundation of China (No. 22379125, 22109030, and 22021001), the Fundamental Research Funds for the Central Universities (20720220073), and Fujian Industrial Technology Development and Application Plan (2022I0002). The numerical calculations in this paper were carried out at the Hefei Advanced Computing Center.

Conflict of Interests

The authors declare no conflict of interest.

Data Availability Statement

The data that support the findings of this study are available from the corresponding author upon reasonable request.

Keywords: Aqueous Zn-Br_2 batteries · Degradation mechanism · Dual electrode stabilization · High areal capacity · Polybromide shuttle effect

[1] L. Zhang, J. Huang, H. Guo, L. Ge, Z. Tian, M. Zhang, J. Wang, G. He, T. Liu, J. Hofkens, D. J. L. Brett, F. Lai, *Adv. Energy Mater.* **2023**, *13*, 2203790.
[2] W. Yuan, X. Qu, Y. Wang, X. Li, X. Ru, D. Jia, L. Zhao, Y. Hou, J. Shen, Z. Shen, N. Zhang, *Energy Storage Mater.* **2025**, *76*, 104130.
[3] S. Zheng, L. Wei, Z. Zhang, J. Pan, J. He, L. Gao, C. C. Li, *Nano Lett.* **2022**, *22*, 9062–9070.
[4] J. Sun, X. Zheng, Z. Zhu, M. Wang, Y. Xu, K. Li, Y. Yuan, M. Chuai, Z. Liu, T. Jiang, H. Hu, W. Chen, *Nano Lett.* **2025**, *25*, 7266–7275.
[5] K. Yan, Y. Fan, X. Yang, X. Wang, S. Chen, W. Wang, M. Zhang, H. Fan, L. Ma, *Energy Environ. Sci.* **2025**, *18*, 5333–5346.
[6] J. Yang, S. Wang, L. Du, S. Bi, J. Zhu, L. Liu, Z. Niu, *Adv. Funct. Mater.* **2024**, *34*. 2314426.
[7] C. Liu, W. Dong, H. Zhou, J. Li, H. Du, X. Ji, S. Cheng, *ACS Appl. Mater. Interfaces.* **2024**, *16*, 23278–23287.
[8] Q. Deng, S. You, W. Min, Y. Xu, W. Lin, J. Lu, C. Yang, *Adv. Mater.* **2024**, *36*, 2312924.
[9] M. Wang, J. Ma, Y. Meng, P. Tong, R. Luo, D. Shen, X. Zheng, N. Chen, M. Zhang, L. Song, Z. Zhang, D. Li, C. Wang, H. Cheng, Y. Lu, Z. Li, W. Chen, *eScience.* **2025**, 100397.
[10] M. Liu, W. Yuan, X. Qu, X. Ru, X. Li, T. Wang, X. Wang, Y. Wang, Y. Liu, N. Zhang, *Energy Environ. Sci.* **2024**, *17*, 9611–9622.
[11] X. Wang, Z. Zhang, B. Xi, W. Chen, Y. Jia, J. Feng, S. Xiong, *ACS Nano.* **2021**, *15*, 9244–9272.
[12] X. Zheng, R. Luo, Z. Liu, M. Wang, M. Sajid, Z. Xie, J. Sun, K. Xu, L. Song, Y. Yuan, T. Jiang, S. Liu, N. Chen, W. Chen, *Mater. Today.* **2024**, *80*, 353–364.
[13] S. Lv, T. Fang, Z. Ding, Y. Wang, H. Jiang, C. Wei, D. Zhou, X. Tang, X. Liu, *ACS Nano.* **2022**, *16*, 20389–20399.
[14] S. Wang, Y. Wang, Z. Wei, J. Zhu, Z. Chen, H. Hong, Q. Xiong, D. Zhang, S. Li, S. Wang, Y. Huang, C. Zhi, *Adv. Mater.* **2024**, *36*, 2401924.
[15] X. Zhao, J. Hao, Q. Chen, S.-J. Zhang, H. Wu, L. Mao, S. Qiao, *Angew. Chem. Int. Ed.* **2025**, *64*, e202502386.
[16] S. Chen, C. Peng, D. Zhu, C. Zhi, *Adv. Mater.* **2024**, *36*, 2409810.
[17] W. Li, H. Xu, S. Ke, H. Zhang, H. Chen, G. Guo, X. Xiong, S. Zhang, J. Fu, C. Jing, J. Cheng, S. Liu, *Nano-Micro Lett.* **2025**, *17*, 143.
[18] J. Guo, L. Hu, R. Wang, G. Liu, J. Zhao, C. Dai, Z. Lin, *ACS Nano.* **2025**, *19*, 9340–9350.
[19] W. Wu, S. Xu, Z. Lin, L. Lin, R. He, X. Sun, *Energy Storage Mater.* **2022**, *49*, 11–18.
[20] L. Gao, Z. Li, Y. Zou, S. Yin, P. Peng, Y. Shao, X. Liang, *iScience.* **2020**, *23*, 101348.
[21] J. Yang, Q. Dai, S. Hou, C. Han, L. Zhao, *Adv. Mater.* **2025**, *37*, 2418258.
[22] S. Biswas, A. Senju, R. Mohr, T. Hodson, N. Karthikeyan, K. W. Knehr, A. G. Hsieh, X. Yang, B. E. Koel, D. A. Steingart, *Energy Environ. Sci.* **2017**, *10*, 114–120.
[23] R. M. Darling, K. G. Gallagher, J. A. Kowalski, S. Ha, F. R. Brushett, *Energy Environ. Sci.* **2014**, *7*, 3459–3477.
[24] T. Feng, Z. Zhang, Y. Guo, S. Li, K. Han, Y. Wang, C. Gong, J. Fan, G. Liu, Y. Huang, *Energy Storage Mater.* **2025**, *79*, 104341.
[25] J. Guo, G. Ma, G. Liu, C. Dai, Z. Lin, *Adv. Energy Mater.* **2024**, *14*, 2304516.
[26] J. Zhao, Y. Qi, Y. Chen, M. Zhang, Z. An, W. Wang, B. Nian, Y. Li, S. Han, L. Zhang, *Angew. Chem. Int. Ed.* **2025**, *64*, e202421905.
[27] S. Hee Han, S. Kim, H. Yong Lim, S. Park, K. Shin, S. Kim, H.-T. Kim, S. Kyu Kwak, C. Yang, N.-S. Choi, *Chem. Eng. J.* **2023**, *464*, 142624.
[28] C. Wang, Q. Lai, P. Xu, D. Zheng, X. Li, H. Zhang, *Adv. Mater.* **2017**, *29*, 1605815.
[29] B. Huskinson, M. P. Marshak, C. Suh, S. Er, M. R. Gerhardt, C. J. Galvin, X. Chen, A. Aspuru-Guzik, R. G. Gordon, M. J. Aziz, *Nature.* **2014**, *505*, 195–198.
[30] Y. Zhang, C. Wei, M.-X. Wu, Y. Wang, H. Jiang, G. Zhou, X. Tang, X. Liu, *Chem. Eng. J.* **2023**, *451*, 138915.
[31] H. Wei, G. Qu, X. Zhang, B. Ren, S. Li, J. Jiang, Y. Yang, J. Yang, L. Zhao, H. Li, C. Zhi, Z. Liu, *Energy Environ. Sci.* **2023**, *16*, 4073–4083.
[32] X. Li, N. Li, Z. Huang, Z. Chen, Y. Zhao, G. Liang, Q. Yang, M. Li, Q. Huang, B. Dong, J. Fan, C. Zhi, *ACS Nano.* **2021**, *15*, 1718–1726.
[33] J. Heo, K. Shin, H. Kim, *Adv. Sci.* **2022**, *9*, 2204908.
[34] C. Wang, Q. Xie, G. Wang, Y. Lyu, Q. Wang, X. Ma, H. Wang, T. Guo, Y. Wu, J. Han, *Nano Lett.* **2024**, *24*, 13796–13804.
[35] H. Yang, S. Lin, Y. Qu, G. Wang, S. Xiang, F. Liu, C. Wang, H. Tang, D. Wang, Z. Wang, X. Liu, Y. Zhang, Y. Wu, *Adv. Sci.* **2024**, *11*, 2307780.
[36] C. Xu, C. Lei, P. Jiang, W. Yang, W. Ma, X. He, X. Liang, *Joule.* **2024**, *8*, 461–481.

[37] L. Han, Y. Guo, F. Ning, X. Liu, J. Yi, Q. Luo, B. Qu, J. Yue, Y. Lu, Q. Li, *Adv. Mater.* **2024**, *36*, 2308086.
[38] S. Chen, Y. Ying, S. Wang, L. Ma, H. Huang, X. Wang, X. Jin, S. Bai, C. Zhi, *Angew. Chem. Int. Ed.* **2023**, *62*, e202301467.
[39] S. Chen, S. Li, L. Ma, Y. Ying, Z. Wu, H. Huang, C. Zhi, *Angew. Chem. Int. Ed.* **2024**, *63*, e202319125.
[40] X. Zheng, Z. Liu, J. Sun, R. Luo, K. Xu, M. Si, J. Kang, Y. Yuan, S. Liu, T. Ahmad, T. Jiang, N. Chen, M. Wang, Y. Xu, M. Chuai, Z. Zhu, Q. Peng, Y. Meng, K. Zhang, W. Wang, W. Chen, *Nat. Commun.* **2023**, *14*, 76.
[41] J.-H. Lee, Y. Byun, G. H. Jeong, C. Choi, J. Kwen, R. Kim, I. H. Kim, S. O. Kim, H.-T. Kim, *Adv. Mater.* **2019**, *31*, 1904524.
[42] Q. Wang, Q. Dou, G. Deng, G. Li, Y. Ma, P. Tang, Y. Cui, C. Yang, L. Zang, X. Yan, *J. Mater. Chem. A.* **2024**, *12*, 15658–15665.
[43] L. Hu, C. Dai, Y. Zhu, X. Hou, Z. Liu, X. Geng, H. Wang, J. Chen, N. Sun, Q. Rong, Y. Zhu, X. He, Y. Lin, *Energy Environ. Sci.* **2024**, *17*, 5552–5562.

Manuscript received: June 17, 2025
Revised manuscript received: July 14, 2025
Accepted manuscript online: August 01, 2025
Version of record online: ■■, ■■